Active Tuning of Hybridized Modes in a Heterogeneous Photonic Molecule

Kevin C. Smith,[1] Yueyang Chen,[2] Arka Majumdar,[2,1,†] and David J. Masiello[3,*]

[1] *Department of Physics, University of Washington, Seattle, Washington 98195, USA*
[2] *Department of Electrical and Computer Engineering, University of Washington, Seattle, Washington 98195, USA*
[3] *Department of Chemistry, University of Washington, Seattle, Washington 98195, USA*

(Received 17 December 2019; revised manuscript received 1 March 2020; accepted 20 March 2020; published 15 April 2020)

From fundamental discovery to practical application, advances in the optical and quantum sciences rely upon precise control of light-matter interactions. Systems of coupled optical cavities are ubiquitous in these efforts, yet the design and active modification of the hybridized mode properties remains challenging. Here, we demonstrate the design, fabrication, and analysis of a tunable heterogeneous photonic molecule consisting of a ring resonator strongly coupled to a nanobeam photonic crystal cavity. Leveraging the disparity in mode volume between these two strongly coupled cavities, we combine theory and experiment to establish the ability to actively tune the mode volume of the resulting supermodes over a full order of magnitude. As the mode volume determines the strength of light-matter interactions, this work illustrates the potential for strongly coupled cavities with dissimilar mode volumes in applications requiring designer photonic properties and tunable light-matter coupling, such as photonics-based quantum simulation.

DOI: 10.1103/PhysRevApplied.13.044041

I. INTRODUCTION

Coupled optical microcavities serve as a basic building block for many integrated photonic systems and technologies. Similar to the way in which bound electronic states of individual atoms couple to form those of a molecule, confined photonic excitations of two or more optical cavities can electromagnetically interact to form so-called "photonic molecules" [1–6]. Electronic excitations in molecules are described through hybridization of the orbitals of the constituent atoms and, by analogy, the electromagnetic supermodes of photonic molecules can be constructed by blending the resonances of the individual cavities. While single cavities are instrumental to a diverse set of applications ranging from single-photon generation [7–10] and strong light-matter coupling [11–14] to sensing [15–23] and cavity-controlled chemistry [24–29], systems of two or more cavities have shown promise in a number of applications, including low-threshold lasing [30–32], cavity optomechanics [33–35], nonclassical light generation [36–42], quantum simulation [43–47], and biochemical sensing [48,49].

Critical to the advantages of photonic molecules over individual cavities is the ability to engineer designer supermodes with properties that differ from those of the constituent components. Of particular interest are coupled-cavity structures, the optical properties of which evolve with tunable parameters such as cavity-cavity separation and detuning. In recent years, the active tuning of such photonic molecules has been demonstrated in several experiments [6,35,50] but all have focused on coupled structures composed of near-identical individual cavities. While these devices are useful for many applications, homogeneity of the constituent cavities limits the dynamic range of the resulting supermode properties, such as the mode volume, which is important both for the scaling of light-matter coupling and for Purcell enhancement.

In contrast, a heterogeneous photonic molecule composed of two distinctly different cavities allows for a richer set of emergent properties with a wider scope of applications, such as improved single-photon indistinguishability of quantum emitters [41,42]. However, the lack of a theoretical framework analogous to molecular orbital theory that is capable of elucidating the dependencies of the composite system upon single-cavity parameters makes the design and analysis of coupled optical cavities difficult. Absent such a formalism, the prediction of supermode field profiles and other downstream properties such as hybridized resonant frequencies and mode volumes must be left to numerical simulation. The latter can be costly for all but the simplest coupled cavities and impossible for many heterogeneous systems, providing impetus for theoretical advances in understanding cavity-mode hybridization.

In this work, we demonstrate thermally tunable hybridization of optical cavity modes in a heterogeneous photonic molecule composed of a ring resonator and a

*masiello@uw.edu
†arka@uw.edu

nanobeam photonic crystal (PhC) cavity. This is achieved by embedding the coupled-cavity structure in a high thermo-optic coefficient polymer that preferentially blue shifts the nanobeam resonance relative to the ring due to the "air-mode" design of the PhC cavity [51]. To better understand the resulting supermodes of this heterogeneous optical system, we introduce a theoretical framework that provides rigorous underpinnings to the more familiar coupled-mode theory for hybridized cavity systems and we derive analytical expressions for the supermode field profiles and mode volumes expressed in terms of the single-cavity field profiles. Using this formalism, we demonstrate the ability to extract crucial system parameters, such as the bare resonant frequencies and couplings, as a function of the temperature-dependent detuning. Lastly, we use this theory to predict the evolution of the resonant frequencies, field profiles, and hybridized mode volumes of the two supermodes, revealing a temperature-dependent progression that spans a full order of magnitude and results in the coalescence of the two mode volumes near zero detuning.

II. RESULTS

A. Experiment

Figure 1(a) displays a scanning-electron-microscope (SEM) image of the heterogeneous coupled-cavity system fabricated on a 220-nm-thick silicon-nitride film, grown on thermal oxide on a silicon substrate. The pattern is defined by e-beam lithography and reactive ion etching [52]. The nanobeam cavity is designed such that a significant portion of the cavity field is concentrated in SU-8 polymer, which both forms a cladding for the entire device and fills the holes of the PhC [51] [see Fig. 1(b)]. In contrast, the ring-resonator mode is predominantly confined within the silicon nitride. Due to the relatively high thermo-optic coefficient of the polymer (approximately $-10^{-4}/°\mathrm{C}$), which is nearly an order of magnitude larger than that of silicon nitride, heating the entire device leads to a blue shift of the nanobeam-cavity mode relative to that of the ring. The detuning between the ring and nanobeam modes can therefore be reversibly controlled by changing the temperature.

To investigate the effect of ring–nanobeam-mode detuning, the transmission spectrum is measured through the nanobeam PhC cavity for a range of temperatures spanning $33.5 - 73.5\,°\mathrm{C}$. The spectra are measured using a supercontinuum laser that is coupled to the system via an on-chip grating [see Fig. 1(a)]. The transmitted light is collected through the opposite grating and is sent to the spectrometer. While the gratings already provide a spatial separation to improve the signal-to-noise ratio, a pinhole is used in the confocal microscopy setup to collect light

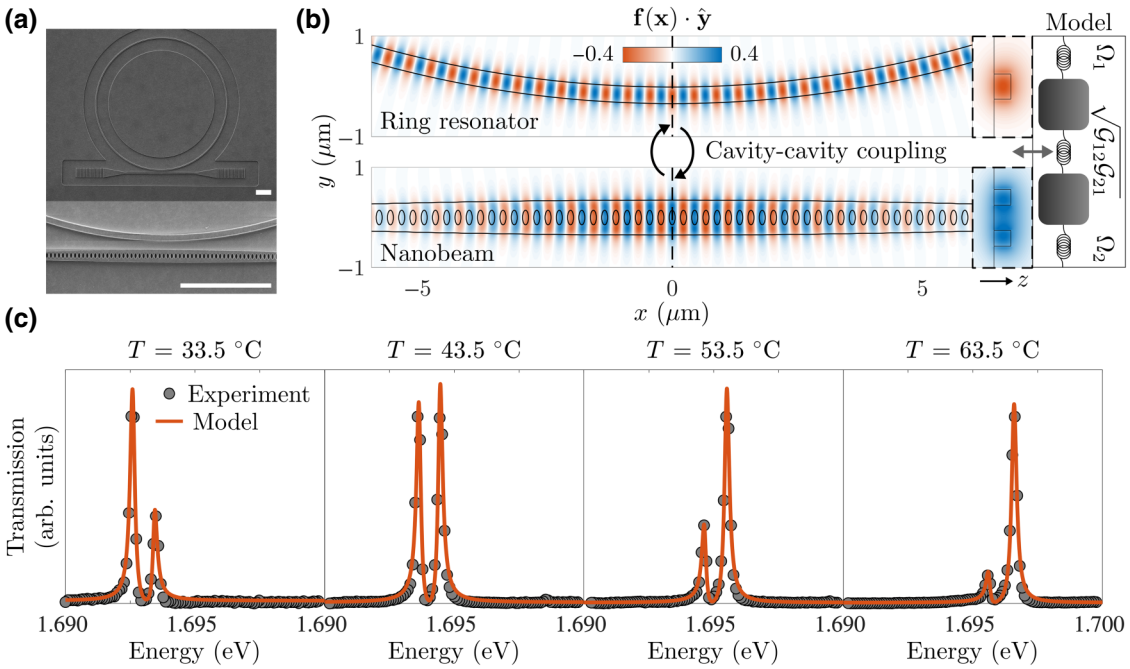

FIG. 1. (a) A SEM image of the SU-8 cladded coupled ring-resonator–nanobeam device with a 500-nm gap between the ring and the nanobeam at the point of closest separation. Scale bar: 5 μm. (b) The y component of the electric field profiles for the nanobeam-cavity mode (bottom) and the ring-resonator mode (top) studied. The system is modeled as a coupled oscillator, parametrized by an effective coupling strength $\sqrt{\mathcal{G}_{12}\mathcal{G}_{21}}$ and effective frequencies Ω_i distinct from the bare resonant frequencies ω_i. (c) Transmission spectra collected for four equally spaced temperatures (gray circles) with simultaneous least-squares fits to the model overlaid (red lines).

only from the output grating. The temperature of the entire chip is controlled using a hot plate. Figure 1(c) displays the resulting transmission spectra (gray circles) for a subset of temperatures, with additional measurements included in the Supplemental Material [53]. As the cavity modes of the ring and nanobeam are coupled, it is difficult to distinguish how much of the energy separation between transmission peaks at each temperature is due to detuning versus mode splitting resulting from coupling.

An understanding of the impact of these individual contributions and analysis of emergent properties requires a theoretical formalism capable of describing the supermodes of the coupled ring-nanobeam structure. Coupled-mode theory provides one such approach but typically relies on several phenomenological rates that simplify the modeling, often at the expense of oversimplifying the underlying physics. Furthermore, coupled-mode theory does not provide a means to predict supermode properties of interest for heterogeneous photonic molecules, such as hybridized mode volumes. To amend these deficiencies, we develop a first-principles theory that provides analytical understanding of the supermode resonant frequencies, field profiles, and volumes based only upon knowledge of the individual uncoupled cavities.

B. Theoretical model

The resonant modes of an optical cavity are given by the independent harmonic solutions of the wave equation

$$\nabla \times \nabla \times \mathbf{A}(\mathbf{x},t) + \frac{\varepsilon(\mathbf{x})}{c^2}\ddot{\mathbf{A}}(\mathbf{x},t) = \mathbf{0}, \tag{1}$$

where $\mathbf{A}$ is the vector potential related to the cavity fields by the usual relations $\mathbf{E} = -\dot{\mathbf{A}}/c$ and $\mathbf{B} = \nabla \times \mathbf{A}$, $\varepsilon(\mathbf{x})$ is the dielectric function of the structure of interest, and c is the speed of light. As is typical for cavity quantum-electrodynamics calculations, we work entirely in the generalized Coulomb gauge defined by $\nabla \cdot \varepsilon(\mathbf{x})\mathbf{A}(\mathbf{x}) = 0$, which leads to a vanishing scalar potential for systems without free charge [54,55]. While optical cavities may alternatively be described at the level of the fields themselves, the vector potential accommodates a more natural basis for both a Lagrangian formulation of the cavity dynamics and canonical quantization [56].

Given $\varepsilon(\mathbf{x})$, it is in principle straightforward to numerically solve for the modes of the two-cavity structure in Fig. 1(a). Such an approach, however, offers limited predictivity and insight into the interaction between the individual ring resonator and nanobeam modes. In addition, the vastly different length scales of the ring resonator and nanobeam cavity make electromagnetic simulations of the coupled structures computationally challenging, rendering a purely numerical exploration of parameter space infeasible. A more flexible strategy is to numerically solve for the modes of the individual uncoupled cavities. With the aid of analytics, these individual modes may then be appropriately mixed to form supermodes dependent on basic system parameters such as the spectral detuning and the physical separation between the cavities.

Considering just a single-cavity mode of both the ring resonator and nanobeam, the vector potential for the double-cavity structure can be expanded as

$$\mathbf{A}(\mathbf{x},t) = \sum_{i=1,2} \frac{\sqrt{4\pi}c}{V_i} q_i(t)\mathbf{f}_i(\mathbf{x}). \tag{2}$$

Here, $i = 1, 2$ corresponds to the ring and nanobeam, respectively, while $\mathbf{f}_i(\mathbf{x})$ is a mode function of the ith cavity [53] and $q_i(t)$ a time-dependent amplitude. The mode functions are normalized such that the mode volume [57–59] is given by

$$V_i = \frac{\int d^3x\, \varepsilon_i(\mathbf{x})\, |\mathbf{E}_i(\mathbf{x})|^2}{\max[\varepsilon_i(\mathbf{x})\, |\mathbf{E}_i(\mathbf{x})|^2]} = \int d^3x\, \varepsilon_i(\mathbf{x})\, |\mathbf{f}_i(\mathbf{x})|^2 . \tag{3}$$

The mode expansion in Eq. (2) is approximate and, in general, requires additional terms to ensure that Gauss's law is obeyed [60–62]. However, these contributions only become physically relevant at small intercavity separations, where the evanescent field of one cavity "spills" into the dielectric medium composing the other, and therefore may be ignored for the ring–nanobeam-resonator studied [53].

The resonant-supermode frequencies are most easily computed through diagonalization of the equations of motion for the generalized coordinates q_i. The derivation of such equations is straightforward using standard techniques of Lagrangian mechanics (see Appendix A) but an equivalent route involves directly integrating Eq. (1) [63]. Regardless of the approach, the coupled equations of motion are as follows:

$$\frac{d^2}{dt^2}\begin{bmatrix} q_1 \\ q_2 \end{bmatrix} = -\begin{bmatrix} \Omega_1^2 & \mathcal{G}_{12} \\ \mathcal{G}_{21} & \Omega_2^2 \end{bmatrix}\begin{bmatrix} q_1 \\ q_2 \end{bmatrix}, \tag{4}$$

where $\Omega_i^2 = (\bar{\omega}_i^2 - \bar{g}_E\bar{g}_M)/(1 - \bar{g}_E^2/\bar{\omega}_1\bar{\omega}_2)$ and $\mathcal{G}_{ij} = \sqrt{\bar{\omega}_j\,\bar{V}_i/\bar{\omega}_i\bar{V}_j}\left(\bar{\omega}_i\bar{g}_M - \bar{\omega}_j\bar{g}_E\right)/(1 - \bar{g}_E^2/\bar{\omega}_1\bar{\omega}_2)$ define effective resonant frequencies and couplings.

These coupled equations of motion differ from those often assumed in the application of coupled-mode theory to multiple-cavity systems [6,64,65]. In particular, the diagonal elements of the above coefficient matrix are distinct from the bare resonance frequencies ω_i. This is a consequence of the absence of a weak-coupling approximation, resulting in coupling-induced resonance shifts [66] that scale as higher-order products of the three distinct coupling parameters corresponding to the electric (g_E) and

magnetic (g_M) intercavity couplings and the polarization-induced intracavity self-interaction (Σ_i), defined by

$$\begin{aligned} g_E &= \sqrt{\frac{\omega_1\omega_2}{V_1V_2}}\int d^3x\,\varepsilon(\mathbf{x})\mathbf{f}_1(\mathbf{x})\cdot\mathbf{f}_2(\mathbf{x}),\\ g_M &= \frac{1}{2}\sqrt{\frac{1}{\omega_1\omega_2V_1V_2}}\int d^3x\,\left[\omega_1^2\varepsilon_1(\mathbf{x})+\omega_2^2\varepsilon_2(\mathbf{x})\right]\\ &\quad\times\mathbf{f}_1(\mathbf{x})\cdot\mathbf{f}_2(\mathbf{x}),\\ \Sigma_i &= \sqrt{\frac{1}{V_1V_2}}\int d^3x\,\left[\varepsilon(\mathbf{x})-\varepsilon_i(\mathbf{x})\right]|\mathbf{f}_i(\mathbf{x})|^2\,. \end{aligned} \tag{5}$$

The intracavity self-interaction Σ_i does not explicitly appear in Eq. (4), as all intercavity couplings, resonant frequencies (ω_i), and mode volumes (V_i) are replaced by renormalized counterparts (indicated by a bar), defined explicitly in Appendix A.

While coupled-mode theory often reduces cavity-mode interactions to a single coupling parameter independent of the detuning, we note that this is not completely accurate and that more rigorous first-principles treatments relying on tight-binding methods [63,67] have revealed three distinct coupling parameters, in agreement with those defined above. However, as shown in Eq. (4), these three parameters may be combined, along with the resonant frequencies, to form effective coupled-oscillator equations that account for these subtleties. Notably, all parameters may be computed given only the dielectric function composing the individual cavities along with associated field mode profiles.

C. Fit to experimental data

Aided by the effective oscillator equations in Eq. (4), the transmission spectrum is derived through standard input-output methods [53,64,68], yielding

$$\mathcal{T}(\omega) = \left|\frac{\kappa}{\omega-\Omega_1+i\kappa+\dfrac{\mathcal{G}_{12}\mathcal{G}_{21}/4\Omega_1\Omega_2}{\omega-\Omega_2}}\right|^2. \tag{6}$$

Simultaneous least-squares fits are performed to transmission spectra at the eight experimentally probed temperatures shown in Fig. 1(c) and the Supplemental Material [53]. To minimize the number of free parameters, Σ_1, Σ_2, V_1, and V_2 are calculated using the theory, supplemented by numerically calculated single-cavity field profiles. Similarly, g_E and g_M are constrained to within $\pm1\%$ of their theoretical values, while the waveguide-induced dissipation rate κ is estimated from electromagnetic simulation of the nanobeam.

The remaining free parameters, displayed in the top row of Table I, are extracted through a simultaneous least-squares fit to all measured transmission spectra. Among them are the resonant frequencies of both the ring resonator and the nanobeam at room temperature T_0 and associated intrinsic dissipation rates, the latter of which may be introduced via input-output theory in the standard way by generalizing Ω_1 and Ω_2 to be complex valued [64]. We find that the temperature dependence of the resonant wavelength of each cavity is well approximated as linear. All other parameters are assumed to depend negligibly upon temperature and are treated as constant. Even with these simplifying approximations, agreement between experiment (circles) and theory (solid lines) is excellent, as is evident in Fig. 1(c).

Figure 2(a) displays the full set of transmission measurements (circles) and fits (curves) for all eight probed temperatures, while Fig. 2(b) shows the supermode resonant frequencies ($\omega_\pm$) as a function of the energy detuning $\hbar\omega_2-\hbar\omega_1$. For each temperature measured, the resonant frequencies are estimated from the peaks in the transmission spectra and are shown as black circles. The theory curves (red and blue) are computed through diagonalization of the effective oscillator model in Eq. (4), which we parametrize according to Table I. Because both the ring and nanobeam modes blue shift with increasing temperature, the plotted curves and points are shifted with respect to the average resonant energy $\omega_{\text{avg}}=(\omega_++\omega_-)/2$ for both panels.

The resonant frequencies undergo an anticrossing as the system nears zero detuning around $T=40^\circ$C, with the upper- and lower-cavity-polariton energies differing by approximately 0.8 meV. Because the coupled-oscillator model is parametrized by the effective frequencies Ω_1 and

TABLE I. Parameter estimates.

$\hbar\omega_1(T_0)$	$\hbar\omega_2(T_0)$	$d\lambda_1/dT$	$d\lambda_2/dT$	$\hbar\gamma_1$	$\hbar\gamma_2$	
1.6922 eV	1.6918 eV	−39 pm/°nC	−50 pm/°nC	0.16 meV	0.23 meV	
V_1	V_2	κ	$\hbar g_E$	$\hbar g_M$	Σ_1	Σ_2
5.0 μm^3	0.49 μm^3	9.7 μeV	−16.4 meV	−15.6 meV	1.1×10^{-5}	8.5×10^{-5}

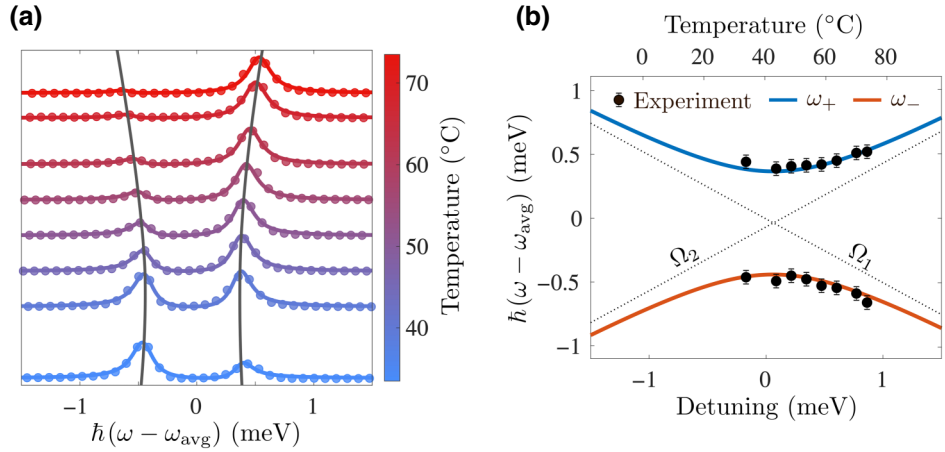

FIG. 2. (a) Anticrossing resulting from strong coupling between the ring-resonator and nanobeam-cavity modes. Experimental data are shown as circles, while colored solid lines display the resulting least-squares fit to Eq. (6). The gray lines overlie the theoretical values of $\omega_\pm$, extrapolated via parameter values obtained from the fits. (b) The evolution of the supermode resonant frequencies as a function of the detuning. The black points correspond to experimentally measured peak transmission energies, while the error bars indicate the uncertainty in the peak energy due to the finite density of the transmission energies measured. The solid curves display the theoretical supermode energies computed from Eq. (4), parametrized through simultaneous fits to transmission measurements.

Ω_2, and not the bare-cavity resonances ω_1 and ω_2, the anticrossing occurs where the former, and not the latter, are coresonant. Thus, the anticrossing in Fig. 2 is slightly shifted from zero detuning. In addition, the supermode resonances $\omega_\pm$ tend toward the effective frequencies (dotted lines) at large positive and negative values of the detuning. Strong coupling is confirmed quantitatively through comparison of the computed effective coupling strength [53] with the dissipation rates reported in Table I [69,70]. In particular, we find that $\left|\hbar\sqrt{\mathcal{G}_{12}\mathcal{G}_{21}/4\Omega_1\Omega_2}\right| \approx 0.40$ meV, nearly double the dominant intrinsic dissipation rate $\hbar\gamma_1 = 0.23$ meV.

D. Analysis of supermode properties

Hybridization is further investigated through inspection of the supermode profiles

$$\mathbf{f}_\mp(\mathbf{x}) = \frac{1}{A(\theta)}\left[\left(\frac{\mathcal{G}_{12}}{\mathcal{G}_{21}}\right)^{1/4}\sqrt{\frac{V_2}{V_1}}\mathbf{f}_1(\mathbf{x})\cos\theta - \left(\frac{\mathcal{G}_{21}}{\mathcal{G}_{12}}\right)^{1/4}\sqrt{\frac{V_1}{V_2}}\mathbf{f}_2(\mathbf{x})\sin\theta\right],$$
$$\mathbf{f}_\pm(\mathbf{x}) = \frac{1}{B(\theta)}\left[\left(\frac{\mathcal{G}_{21}}{\mathcal{G}_{12}}\right)^{1/4}\sqrt{\frac{V_1}{V_2}}\mathbf{f}_2(\mathbf{x})\cos\theta + \left(\frac{\mathcal{G}_{12}}{\mathcal{G}_{21}}\right)^{1/4}\sqrt{\frac{V_2}{V_1}}\mathbf{f}_1(\mathbf{x})\sin\theta\right], \quad (7)$$

and their associated mode volumes

$$V_\mp = V_1\left[\frac{V_2}{V_1}\sqrt{\frac{\mathcal{G}_{12}}{\mathcal{G}_{21}}}\frac{1+\Sigma_1}{A(\theta)^2}\right]\cos^2\theta + V_2\left[\frac{V_1}{V_2}\sqrt{\frac{\mathcal{G}_{21}}{\mathcal{G}_{12}}}\frac{1+\Sigma_2}{A(\theta)^2}\right]\sin^2\theta - \sqrt{V_1V_2}\left[\frac{g_E/\sqrt{\omega_1\omega_2}}{A(\theta)^2}\right]\sin 2\theta,$$
$$V_\pm = V_2\left[\frac{V_1}{V_2}\sqrt{\frac{\mathcal{G}_{21}}{\mathcal{G}_{12}}}\frac{1+\Sigma_2}{B(\theta)^2}\right]\cos^2\theta + V_1\left[\frac{V_2}{V_1}\sqrt{\frac{\mathcal{G}_{12}}{\mathcal{G}_{21}}}\frac{1+\Sigma_1}{B(\theta)^2}\right]\sin^2\theta + \sqrt{V_1V_2}\left[\frac{g_E/\sqrt{\omega_1\omega_2}}{B(\theta)^2}\right]\sin 2\theta, \quad (8)$$

where $A(\theta)$ and $B(\theta)$ are normalization factors defined by Ref. [53]

$$A(\theta)^2 = \mathrm{Max}\left\{\varepsilon(\mathbf{x})\left[\left(\frac{\mathcal{G}_{12}}{\mathcal{G}_{21}}\right)^{1/4}\sqrt{\frac{V_2}{V_1}}\mathbf{f}_1(\mathbf{x})\cos\theta + \left(\frac{\mathcal{G}_{21}}{\mathcal{G}_{12}}\right)^{1/4}\sqrt{\frac{V_1}{V_2}}\mathbf{f}_2(\mathbf{x})\sin\theta\right]^2\right\},$$

$$B(\theta)^2 = \mathrm{Max}\left\{\varepsilon(\mathbf{x})\left[\left(\frac{\mathcal{G}_{21}}{\mathcal{G}_{12}}\right)^{1/4}\sqrt{\frac{V_1}{V_2}}\,\mathbf{f}_2(\mathbf{x})\cos\theta - \left(\frac{\mathcal{G}_{12}}{\mathcal{G}_{21}}\right)^{1/4}\sqrt{\frac{V_2}{V_1}}\,\mathbf{f}_1(\mathbf{x})\sin\theta\right]^2\right\}, \tag{9}$$

$\theta = (1/2)\tan^{-1}(2\sqrt{\mathcal{G}_{12}\mathcal{G}_{21}}/[\Omega_2^2 - \Omega_1^2])$ is the mixing angle, and the upper (lower) subscript corresponds to the case $\theta > 0$ ($\theta < 0$). The mixing angle has two distinct regimes; when the detuning is much larger than the effective coupling strength ($\theta \to 0$), the above mode functions reduce to those of the bare ring resonator and nanobeam cavity. In contrast, for small detuning relative to the coupling ($\theta \to \pm\pi/4$), the mode functions become a superposition of $\mathbf{f}_1(\mathbf{x})$ and $\mathbf{f}_2(\mathbf{x})$.

Figure 3(a) shows the evolution of the y component of the upper- (top) and lower- (bottom) cavity-polariton field profiles across the experimentally measured temperature range. Because the limits of this range constrain the mixing angle to $-\pi/8 \lesssim \theta \lesssim \pi/6$, neither $\mathbf{f}_+(\mathbf{x})$ nor $\mathbf{f}_-(\mathbf{x})$ entirely localize to one of the constituent cavities at any probed temperature. For all mode profiles shown, a significant portion of the field is contributed by the mode function of the nanobeam $\mathbf{f}_2(\mathbf{x})$. We note, however, that there is no fundamental reason why the device could not be heated past the maximum temperature studied here (73°C) or cooled below room temperature.

Notably, the supermode profiles are not equal superpositions of $\mathbf{f}_1(\mathbf{x})$ and $\mathbf{f}_2(\mathbf{x})$ near zero detuning ($T = 40$°C). This may be understood by considering the large mismatch in mode volume between the ring-resonator and nanobeam modes ($V_1/V_2 \sim 10$). According to Eq. (7), the nanobeam contribution to both $\mathbf{f}_+(\mathbf{x})$ and $\mathbf{f}_-(\mathbf{x})$ scales like $(V_1/V_2)^{1/4}$, while that of the ring resonator scales like $(V_2/V_1)^{1/4}$. As a result, both supermodes are predominantly localized to the nanobeam.

Figure 3(b) shows theoretical predictions for the hybridized mode volumes as a function of the temperature-controlled detuning, calculated using Eq. (8) paired with the experimentally informed parameter values in Table I. As before, the blue and red curves correspond to the upper- and lower-cavity polaritons in Fig. 2(a). The gray region indicates the range of experimentally probed temperatures. Both hybridized mode volumes tend toward those of the individual cavities at large positive and negative detuning and coalesce at a value of $V_\pm \approx 0.95\ \mu\mathrm{m}^3$, more than a factor of 5 less than the mode volume of the isolated ring resonator.

While the nanobeam mode volume V_2 clearly serves as a lower bound for $V_\pm$, analysis of Eq. (8) indicates a maximum near $V_1 + V_2$. V_+ slightly exceeds this value due to constructive interference between the two modes, while V_- peaks at a value below $V_1 + V_2$ due to destructive interference. Both mode volumes display a "turning point" at values of the mixing angle θ such that $\mathbf{f}_1(\mathbf{x})$ and $\mathbf{f}_2(\mathbf{x})$ are equally weighted in either $\mathbf{f}_+(\mathbf{x})$ or $\mathbf{f}_-(\mathbf{x})$. Due to the large mismatch between V_1 and V_2, between these two points is a

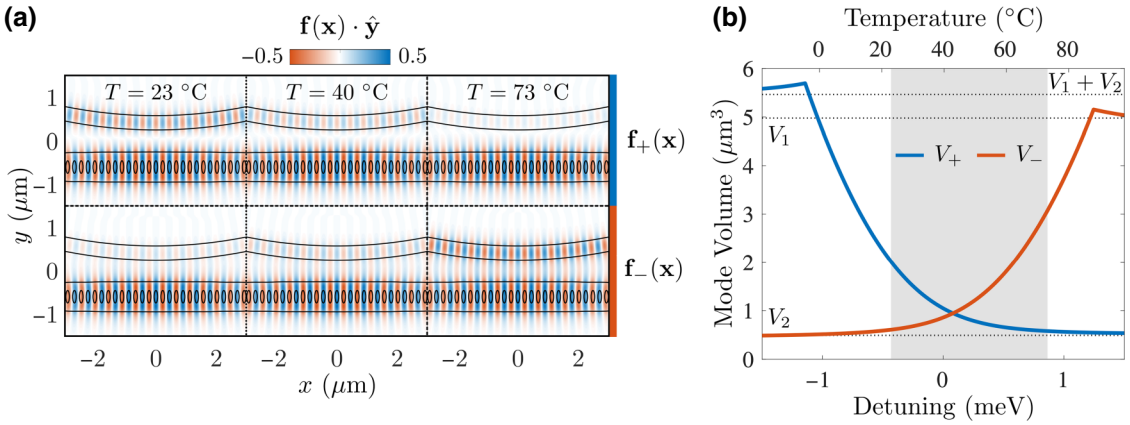

FIG. 3. (a) The field profile for the upper- (top) and lower- (bottom) cavity polaritons at various temperatures. Both supermodes are dominated by the nanobeam field at all observed temperatures due to the weighting of $\mathbf{f}_1(\mathbf{x})$ and $\mathbf{f}_2(\mathbf{x})$ in Eq. (7). (b) The hybridized mode volumes V_+ (blue curve) and V_- (red curve) of the upper- and lower-cavity polaritons. The gray region indicates the range of experimentally measured temperatures, while the dotted lines specify V_1, V_2, and $V_1 + V_2$. Due to the predominant localization of both modes in the nanobeam cavity, both V_+ and V_- coalesce at a value less than 5 times the mode volume of the isolated ring-resonator mode.

full order-of-magnitude of attainable values for both hybridized mode volumes, illustrating the potential of this heterogeneous device for actively tunable photonic properties.

III. CONCLUSION

In conclusion, we demonstrate actively tunable hybridization in a heterogeneous photonic molecule consisting of a ring resonator coupled to a photonic crystal cavity. Critically, we establish an ability to exert control over the coupled cavity's mode volumes, spanning over a full order of magnitude. Aided by a theoretical formalism developed to study hybridized cavity states, we rigorously extract the system parameters from experiment and derive analytical expressions for the supermode resonant frequencies, field profiles, and mode volumes, elucidating their evolution with temperature. As the mode volume is a critical parameter dictating the degree of Purcell enhancement and the scaling of light-matter interaction, these results bear impact upon diverse efforts in the emerging fields of quantum simulation and quantum information processing.

ACKNOWLEDGMENTS

We thank Dr. Xiang-Tian Kong for helpful discussions pertaining to the electromagnetic simulations. This research was supported by the National Science Foundation under the following awards: Grants No. QII-TAQS-1936100 (Y.C., A.M., K.C.S., D.J.M.), No. CHE-1836500 (Y.C., A.M.), No. CHE-1664684 (K.C.S., D.J.M.), and No. CHE-1836506 (K.C.S., D.J.M.). A.M. also acknowledges support from the Sloan Foundation. All fabrication processes were performed at the Washington Nanofabrication Facility, a National Nanotechnology Coordinated Infrastructure site at the University of Washington, which is supported in part by funds from the National Science Foundation (through Awards No. NNCI-1542101, No. 1337840 and No. 0335765), the National Institutes of Health, the Molecular Engineering & Sciences Institute, the Clean Energy Institute, the Washington Research Foundation, the M. J. Murdock Charitable Trust, Altatech, ClassOne Technology, GCE Market, Google, and SPTS.

K. C. S. and Y. C. contributed equally to this paper.

APPENDIX A: DYNAMICS FOR TWO SINGLE-MODE CAVITIES

As mentioned in the main text, the equations of motions for coupled-cavity modes may be computed either through integration of the wave equation [63] or via an Euler-Lagrange approach. Here, we follow the latter strategy and use the standard electromagnetic Lagrangian

$$L = \int \frac{d^3x}{8\pi}\left[\varepsilon(\mathbf{x})\frac{\dot{\mathbf{A}}^2}{c^2} - (\nabla\times\mathbf{A})^2\right] \tag{A1}$$

in the modified Coulomb gauge (and in the absence of free charge). Substituting the expansion Eq. (2) for the vector potential leads to

$$L = \frac{1}{2}\sum_i \frac{\dot{q}_i^2}{V_i}[1+\Sigma_i] - \frac{1}{2}\sum_i \frac{\omega_i^2}{V_i}q_i^2 + \frac{g_E}{\sqrt{\omega_1\omega_2 V_1 V_2}}\dot{q}_1\dot{q}_2 - g_M\sqrt{\frac{\omega_1\omega_2}{V_1V_2}}q_1q_2, \tag{A2}$$

where the analytical forms of g_E, g_M, and Σ_i are given in the main text. Application of the Euler-Lagrange equations then gives

$$\begin{aligned}\frac{\ddot{q}_1}{\bar{V}_1} + \bar{\omega}_1^2\frac{q_1}{\bar{V}_1} + \frac{\bar{g}_E}{\sqrt{\bar{\omega}_1\bar{\omega}_2\bar{V}_1\bar{V}_2}}\ddot{q}_2 + \bar{g}_M\sqrt{\frac{\bar{\omega}_1\bar{\omega}_2}{\bar{V}_1\bar{V}_2}}q_2 = 0,\\ \frac{\ddot{q}_2}{\bar{V}_2} + \bar{\omega}_2^2\frac{q_2}{\bar{V}_2} + \frac{\bar{g}_E}{\sqrt{\bar{\omega}_1\bar{\omega}_2\bar{V}_1\bar{V}_2}}\ddot{q}_1 + \bar{g}_M\sqrt{\frac{\bar{\omega}_1\bar{\omega}_2}{\bar{V}_1\bar{V}_2}}q_1 = 0,\end{aligned} \tag{A3}$$

where the renormalized mode volumes, frequencies, and coupling strengths are defined as follows:

$$\begin{aligned}&\bar{V}_1 = V_1/(1+\Sigma_1) \quad \bar{V}_2 = V_2/(1+\Sigma_2),\\ &\bar{\omega}_1 = \omega_1/\sqrt{1+\Sigma_1} \quad \bar{\omega}_2 = \omega_2/\sqrt{1+\Sigma_2},\\ &\bar{g}_E = g_E/[(1+\Sigma_1)(1+\Sigma_2)]^{3/4},\\ &\bar{g}_M = g_M/[(1+\Sigma_1)(1+\Sigma_2)]^{1/4}.\end{aligned} \tag{A4}$$

Further algebra yields the equations of motion defined in the main text:

$$\frac{d^2}{dt^2}\begin{bmatrix}q_1\\ q_2\end{bmatrix} = -\begin{bmatrix}\Omega_1^2 & \mathcal{G}_{12}\\ \mathcal{G}_{21} & \Omega_2^2\end{bmatrix}\begin{bmatrix}q_1\\ q_2\end{bmatrix}, \tag{A5}$$

where $\Omega_i^2 = (\bar{\omega}_i^2 - \bar{g}_E\bar{g}_M)/(1-\bar{g}_E^2/\bar{\omega}_1\bar{\omega}_2)$ and $\mathcal{G}_{ij} = \sqrt{\bar{\omega}_j\bar{V}_i/\bar{\omega}_i\bar{V}_j}\left(\bar{\omega}_i\bar{g}_M - \bar{\omega}_j\bar{g}_E\right)/(1-\bar{g}_E^2/\bar{\omega}_1\bar{\omega}_2)$.

APPENDIX B: PHYSICAL IMPORTANCE OF THE MODE VOLUME

The mode volume is a critical figure of merit for dielectric cavities, which determines the strength of light-matter interactions [58,59,71]. Here, we show that this remains true in the basis of supermodes of a photonic molecule, lending physical meaning to $V_\pm$. The interaction energy

between a dipole emitter and the two-cavity field is given by

$$H_{\rm int} = -\mathbf{d}\cdot\mathbf{E}(\mathbf{r}_0), \tag{B1}$$

where $\mathbf{d}$ is the dipole moment of the emitter and $\mathbf{r}_0$ is its position. Upon transformation to the supermode basis [53], the field of the cavity may be written as

$$\mathbf{E} = -\frac{\dot{\mathbf{A}}}{c} = -\frac{\sqrt{4\pi}}{V_+}\dot{q}_+(t)\mathbf{f}_+(\mathbf{x}) - \frac{\sqrt{4\pi}}{V_-}\dot{q}_-(t)\mathbf{f}_-(\mathbf{x}). \tag{B2}$$

Substituting this into the interaction Hamiltonian and writing the dipole moment in terms of a generalized coordinate $\mathbf{d} = e\mathbf{x}$,

$$H_{\rm int} = -\frac{e\sqrt{4\pi}}{V_+}[\mathbf{f}_+(\mathbf{r}_0)\cdot\hat{\mathbf{x}}]x\dot{q}_+ - \frac{e\sqrt{4\pi}}{V_-}[\mathbf{f}_-(\mathbf{r}_0)\cdot\hat{\mathbf{x}}]x\dot{q}_-, \tag{B3}$$

which clearly reveals the dependence of the coupling strength on the mode volume $V_\pm$. Importantly, the mode functions are normalized such that $\max[\varepsilon(\mathbf{x})\mathbf{f}_\pm(\mathbf{x})\cdot\mathbf{f}_\pm(\mathbf{x})] = 1$ and therefore the limit $\mathbf{f}_\pm(\mathbf{r}_0)\cdot\hat{\mathbf{x}} \to 1$ corresponds to the case of maximal coupling when $\varepsilon(\mathbf{x})$ is real and dispersionless.

APPENDIX C: EFFECTIVE HAMILTONIAN APPROACH FOR CALCULATION OF TRANSMISSION SPECTRA

Computation of the power transmitted through the coupled ring-nanobeam system is most easily achieved in the basis of creation and annihilation operators. Standard canonical-quantization techniques rely on computation of the Hamiltonian associated with the Lagrangian in Eq. (A2). Due to the coupling between $\dot{q}_1$ and $\dot{q}_2$, however, this leads to conjugate momenta that themselves are coupled in the Hamiltonian. The result of this is that the rotating-wave approximation is no longer valid and standard techniques of input-output theory for coupled systems become ineffective.

The most straightforward path to quantization is via the effective Lagrangian

$$L = \frac{1}{2}\sum_i\left[\frac{\dot{q}_i^2}{\mathcal{V}_i} - \Omega_i^2\frac{q_i^2}{\mathcal{V}_i}\right] - \sqrt{\frac{\mathcal{G}_{12}\mathcal{G}_{21}}{\mathcal{V}_1\mathcal{V}_2}}q_1q_2, \tag{C1}$$

where $1/\mathcal{V}_1 = (\mathcal{G}_{21}/\bar{\omega}_1\bar{\omega}_2)/\sqrt{\bar{V}_1\bar{V}_2}$ and $1/\mathcal{V}_2 = (\mathcal{G}_{12}/\bar{\omega}_1\bar{\omega}_2)/\sqrt{\bar{V}_1\bar{V}_2}$. While different in form from the standard Lagrangian in Eq. (A1), application of the Euler-Lagrange equations yields the exact same equations of motion. Notably, there is no direct coupling between $\dot{q}_1$ and $\dot{q}_2$, significantly simplifying quantization.

The Legendre transform of the above Lagrangian yields the effective Hamiltonian

$$\begin{aligned} H &= \sum_i\left[\frac{\mathcal{V}_i}{2}p_i^2 + \frac{\Omega_i^2}{2\mathcal{V}_i}x_i^2\right] + \sqrt{\frac{\mathcal{G}_{12}\mathcal{G}_{21}}{\mathcal{V}_1\mathcal{V}_2}}q_1q_2 \\ &= \sum_i \hbar\Omega_i a_i^\dagger a_i + \hbar\sqrt{\frac{\mathcal{G}_{12}\mathcal{G}_{21}}{4\Omega_1\Omega_2}}(a_1^\dagger a_2 + a_1 a_2^\dagger), \end{aligned} \tag{C2}$$

where $a_i = \sqrt{\Omega_i/2\hbar\mathcal{V}_i}[x_i + i(\mathcal{V}_i/\Omega_i)p_i]$ and counter-rotating terms are discarded in accordance with the rotating-wave approximation. This procedure also allows us to identify $\sqrt{\mathcal{G}_{12}\mathcal{G}_{21}/4\Omega_1\Omega_2}$ as the "effective coupling strength" to be compared with the dissipation rates in quantitatively testing for strong coupling. The transmission spectrum may then be computed through standard input-output methods [64,68], yielding

$$\mathcal{T}(\omega) = \left|\frac{\kappa}{\omega - \Omega_1 + i\kappa + \dfrac{\mathcal{G}_{12}\mathcal{G}_{21}/4\Omega_1\Omega_2}{\omega - \Omega_2}}\right|^2. \tag{C3}$$

[1] M. Bayer, T. Gutbrod, J. P. Reithmaier, A. Forchel, T. L. Reinecke, P. A. Knipp, A. A. Dremin, and V. D. Kulakovskii, Optical Modes in Photonic Molecules, Phys. Rev. Lett. **81**, 2582 (1998).

[2] T. Mukaiyama, K. Takeda, H. Miyazaki, Y. Jimba, and M. Kuwata-Gonokami, Tight-Binding Photonic Molecule Modes of Resonant Bispheres, Phys. Rev. Lett. **82**, 4623 (1999).

[3] K. A. Atlasov, K. F. Karlsson, A. Rudra, B. Dwir, and E. Kapon, Wavelength and loss splitting in directly coupled photonic-crystal defect microcavities, Opt. Express **16**, 16255 (2008).

[4] K. A. Atlasov, A. Rudra, B. Dwir, and E. Kapon, Large mode splitting and lasing in optimally coupled photonic-crystal microcavities, Opt. Express **19**, 2619 (2011).

[5] A. Majumdar, A. Rundquist, M. Bajcsy, and J. Vučković, Cavity quantum electrodynamics with a single quantum dot coupled to a photonic molecule, Phys. Rev. B **86**, 045315 (2012).

[6] M. Zhang, C. Wang, Y. Hu, A. Shams-Ansari, T. Ren, S. Fan, and M. Lončar, Electronically programmable photonic molecule, Nat. Photonics **13**, 36 (2018).

[7] C. Santori, D. Fattal, J. Vučković, G. S. Solomon, and Y. Yamamoto, Indistinguishable photons from a single-photon device, Nature **419**, 594 (2002).

[8] A. Kuhn, M. Hennrich, and G. Rempe, Deterministic Single-Photon Source for Distributed Quantum Networking, Phys. Rev. Lett. **89**, 067901 (2002).

[9] W.-H. Chang, W.-Y. Chen, H.-S. Chang, T.-P. Hsieh, J.-I. Chyi, and T.-M. Hsu, Efficient Single-Photon Sources Based on Low-Density Quantum Dots in Photonic-Crystal Nanocavities, Phys. Rev. Lett. **96**, 117401 (2006).

[10] K. M. Birnbaum, A. Boca, R. Miller, A. D. Boozer, T. E. Northup, and H. J. Kimble, Photon blockade in an optical cavity with one trapped atom, Nature **436**, 87 (2005).

[11] C. Weisbuch, M. Nishioka, A. Ishikawa, and Y. Arakawa, Observation of the Coupled Exciton-Photon Mode Splitting in a Semiconductor Quantum Microcavity, Phys. Rev. Lett. **69**, 3314 (1992).

[12] D. G. Lidzey, D. D. C. Bradley, M. S. Skolnick, T. Virgili, S. Walker, and D. M. Whittaker, Strong exciton-photon coupling in an organic semiconductor microcavity, Nature **395**, 53 (1998).

[13] J. P. Reithmaier, G. Sęk, A. Löffler, C. Hofmann, S. Kuhn, S. Reitzenstein, L. V. Keldysh, V. D. Kulakovskii, T. L. Reinecke, and A. Forchel, Strong coupling in a single quantum dot-semiconductor microcavity system, Nature **432**, 197 (2004).

[14] E. Peter, P. Senellart, D. Martrou, A. Lemaître, J. Hours, J. M. Gérard, and J. Bloch, Exciton-Photon Strong-Coupling Regime for a Single Quantum Dot Embedded in a Microcavity, Phys. Rev. Lett. **95**, 067401 (2005).

[15] J. McKeever, J. R. Buck, A. D. Boozer, and H. J. Kimble, Determination of the Number of Atoms Trapped in an Optical Cavity, Phys. Rev. Lett. **93**, 143601 (2004).

[16] T. Fischer, P. Maunz, P. W. H. Pinkse, T. Puppe, and G. Rempe, Feedback on the Motion of a Single Atom in an Optical Cavity, Phys. Rev. Lett. **88**, 163002 (2002).

[17] Ş. K. Özdemir, J. Zhu, X. Yang, B. Peng, H. Yilmaz, L. He, F. Monifi, S. H. Huang, G. L. Long, and L. Yang, Highly sensitive detection of nanoparticles with a self-referenced and self-heterodyned whispering-gallery Raman microlaser, Proc. Natl. Acad. Sci. **111**, E3836 (2014).

[18] F. Vollmer and S. Arnold, Whispering-gallery-mode biosensing: Label-free detection down to single molecules, Nat. Methods **5**, 591 (2008).

[19] F. Vollmer and L. Yang, Label-free detection with high-Q microcavities: A review of biosensing mechanisms for integrated devices, Nanophotonics **1**, 267 (2012).

[20] J. Zhu, Ş. K. Özdemir, Y.-F. Xiao, L. Li, L. He, D.-R. Chen, and L. Yang, On-chip single nanoparticle detection and sizing by mode splitting in an ultrahigh-Q microresonator, Nat. Photonics **4**, 46 (2010).

[21] F. Vollmer, S. Arnold, and D. Keng, Single virus detection from the reactive shift of a whispering-gallery mode, Proc. Natl. Acad. Sci. **105**, 20701 (2008).

[22] L. He, Ş. K. Özdemir, J. Zhu, W. Kim, and L. Yang, Detecting single viruses and nanoparticles using whispering gallery microlasers, Nat. Nanotechnol. **6**, 428 (2011).

[23] K. D. Heylman, N. Thakkar, E. H. Horak, S. C. Quillin, C. Cherqui, K. A. Knapper, D. J. Masiello, and R. H. Goldsmith, Optical microresonators as single-particle absorption spectrometers, Nat. Photonics **10**, 788 (2016).

[24] F. Herrera and F. C. Spano, Cavity-Controlled Chemistry in Molecular Ensembles, Phys. Rev. Lett. **116**, 238301 (2016).

[25] A. D. Dunkelberger, B. T. Spann, K. P. Fears, B. S. Simpkins, and J. C. Owrutsky, Modified relaxation dynamics and coherent energy exchange in coupled vibration-cavity polaritons, Nat. Commun. **7**, 13504 (2016).

[26] A. Thomas, L. Lethuillier-Karl, K. Nagarajan, R. M. A. Vergauwe, J. George, T. Chervy, A. Shalabney, E. Devaux, C. Genet, J. Moran, and T. W. Ebbesen, Tilting a ground-state reactivity landscape by vibrational strong coupling, Science **363**, 615 (2019).

[27] C. Schäfer, M. Ruggenthaler, H. Appel, and A. Rubio, Modification of excitation and charge transfer in cavity quantum-electrodynamical chemistry, Proc. Natl. Acad. Sci. **116**, 4883 (2019).

[28] M. Du, R. F. Ribeiro, and J. Yuen-Zhou, Remote control of chemistry in optical cavities, Chem **5**, 1167 (2019).

[29] J. Lather, P. Bhatt, A. Thomas, T. W. Ebbesen, and J. George, Cavity catalysis by cooperative vibrational strong coupling of reactant and solvent molecules, Angew. Chem. Int. Ed. **58**, 10635 (2019).

[30] A. Nakagawa, S. Ishii, and T. Baba, Photonic molecule laser composed of GaInAsP microdisks, Appl. Phys. Lett. **86**, 041112 (2005).

[31] S. V. Boriskina, Theoretical prediction of a dramatic Q-factor enhancement and degeneracy removal of whispering gallery modes in symmetrical photonic molecules, Opt. Lett. **31**, 338 (2006).

[32] E. I. Smotrova, A. I. Nosich, T. M. Benson, and P. Sewell, Threshold reduction in a cyclic photonic molecule laser composed of identical microdisks with whispering-gallery modes, Opt. Lett. **31**, 921 (2006).

[33] X. Jiang, Q. Lin, J. Rosenberg, K. Vahala, and O. Painter, High-Q double-disk microcavities for cavity optomechanics, Opt. Express **17**, 20911 (2009).

[34] Y.-W. Hu, Y.-F. Xiao, Y.-C. Liu, and Q. Gong, Optomechanical sensing with on-chip microcavities, Front. Phys. **8**, 475 (2013).

[35] C. Cao, S.-C. Mi, Y.-P. Gao, L.-Y. He, D. Yang, T.-J. Wang, R. Zhang, and C. Wang, Tunable high-order sideband spectra generation using a photonic molecule optomechanical system, Sci. Rep. **6**, 22920 (2016).

[36] T. C. H. Liew and V. Savona, Single Photons from Coupled Quantum Modes, Phys. Rev. Lett. **104**, 183601 (2010).

[37] M. Bamba, A. Imamoğlu, I. Carusotto, and C. Ciuti, Origin of strong photon antibunching in weakly nonlinear photonic molecules, Phys. Rev. A **83**, 021802(R) (2011).

[38] D. Gerace and V. Savona, Unconventional photon blockade in doubly resonant microcavities with second-order nonlinearity, Phys. Rev. A **89**, 031803(R) (2014).

[39] H. Flayac and V. Savona, Unconventional photon blockade, Phys. Rev. A **96**, 053810 (2017).

[40] A. Dousse, J. Suffczyński, A. Beveratos, O. Krebs, A. Lemaître, I. Sagnes, J. Bloch, P. Voisin, and P. Senellart, Ultrabright source of entangled photon pairs, Nature **466**, 217 (2010).

[41] A. Saxena, Y. Chen, A. Ryou, C. G. Sevilla, P. Xu, and A. Majumdar, Improving indistinguishability of single photons from colloidal quantum dots using nanocavities, ACS Photonics **6**, 3166 (2019).

[42] H. Choi, D. Zhu, Y. Yoon, and D. Englund, Cascaded Cavities Boost the Indistinguishability of Imperfect Quantum Emitters, Phys. Rev. Lett. **122**, 183602 (2019).

[43] D. G. Angelakis, M. F. Santos, and S. Bose, Photon-blockade-induced Mott transitions and XY spin models in coupled cavity arrays, Phys. Rev. A **76**, 031805(R) (2007).

[44] D. L. Underwood, W. E. Shanks, J. Koch, and A. A. Houck, Low-disorder microwave cavity lattices for quantum simulation with photons, Phys. Rev. A **86**, 023837 (2012).
[45] A. Majumdar, A. Rundquist, M. Bajcsy, V. D. Dasika, S. R. Bank, and J. Vučković, Design and analysis of photonic crystal coupled cavity arrays for quantum simulation, Phys. Rev. B **86**, 195312 (2012).
[46] I. M. Georgescu, S. Ashhab, and F. Nori, Quantum simulation, Rev. Mod. Phys. **86**, 153 (2014).
[47] M. J. Hartmann, Quantum simulation with interacting photons, J. Opt. **18**, 104005 (2016).
[48] S. V. Boriskina, Spectrally engineered photonic molecules as optical sensors with enhanced sensitivity: A proposal and numerical analysis, J. Opt. Soc. Am. B **23**, 1565 (2006).
[49] S. V. Boriskina and L. D. Negro, Self-referenced photonic molecule bio(chemical) sensor, Opt. Lett. **35**, 2496 (2010).
[50] B. Peng, Ş. K. Özdemir, F. Lei, F. Monifi, M. Gianfreda, G. L. Long, S. Fan, F. Nori, C. M. Bender, and L. Yang, Parity-time-symmetric whispering-gallery microcavities, Nat. Phys. **10**, 394 (2014).
[51] Y. Chen, J. Whitehead, A. Ryou, J. Zheng, P. Xu, T. Fryett, and A. Majumdar, Large thermal tuning of a polymer-embedded silicon nitride nanobeam cavity, Opt. Lett. **44**, 3058 (2019).
[52] T. K. Fryett, Y. Chen, J. Whitehead, Z. M. Peycke, X. Xu, and A. Majumdar, Encapsulated silicon nitride nanobeam cavity for hybrid nanophotonics, ACS Photonics **5**, 2176 (2018).
[53] See the Supplemental Material at http://link.aps.org/supplemental/10.1103/PhysRevApplied.13.044041 for spectra and fits for all probed temperatures, theoretical formalism pertaining to both single and coupled cavities, and derivations of supermode resonant frequencies, mode profiles, and mode volumes.
[54] R. J. Glauber and M. Lewenstein, Quantum optics of dielectric media, Phys. Rev. A **43**, 467 (1991).
[55] B. J. Dalton, E. S. Guerra, and P. L. Knight, Field quantization in dielectric media and the generalized multipolar Hamiltonian, Phys. Rev. A **54**, 2292 (1996).
[56] C. Cohen-Tannoudji, J. Dupont-Roc, and G. Grynberg, *Photons and Atoms: Introduction to Quantum Electrodynamics* (Wiley, Weinheim, Germany, 1997).
[57] O. Painter, Two-dimensional photonic band-gap defect mode laser, Science **284**, 1819 (1999).
[58] D. Englund, D. Fattal, E. Waks, G. Solomon, B. Zhang, T. Nakaoka, Y. Arakawa, Y. Yamamoto, and J. Vučković, Controlling the Spontaneous Emission Rate of Single Quantum Dots in a Two-Dimensional Photonic Crystal, Phys. Rev. Lett. **95**, 013904 (2005).
[59] P. Lodahl, S. Mahmoodian, and S. Stobbe, Interfacing single photons and single quantum dots with photonic nanostructures, Rev. Mod. Phys. **87**, 347 (2015).
[60] S. G. Johnson, M. Ibanescu, M. A. Skorobogatiy, O. Weisberg, J. D. Joannopoulos, and Y. Fink, Perturbation theory for Maxwell's equations with shifting material boundaries, Phys. Rev. E **65**, 066611 (2002).
[61] K. C. Smith, Y. Chen, A. Majumdar, and D. Masiello, (unpublished).
[62] G. Fisicaro, L. Genovese, O. Andreussi, N. Marzari, and S. Goedecker, A generalized Poisson and Poisson-Boltzmann solver for electrostatic environments, J. Chem. Phys. **144**, 014103 (2016).
[63] A. Yariv, Y. Xu, R. K. Lee, and A. Scherer, Coupled-resonator optical waveguide: A proposal and analysis, Opt. Lett. **24**, 711 (1999).
[64] H. A. Haus, *Waves and Fields in Optoelectronics* (Prentice-Hall, Englewood Cliffs, NJ, 1984).
[65] Q. Li, T. Wang, Y. Su, M. Yan, and M. Qiu, Coupled mode theory analysis of mode-splitting in coupled cavity system, Opt. Express **18**, 8367 (2010).
[66] M. Popovic, C. Manolatou, and M. Watts, Coupling-induced resonance frequency shifts in coupled dielectric multi-cavity filters, Opt. Express **14**, 1208 (2006).
[67] M. Bayindir, B. Temelkuran, and E. Ozbay, Tight-Binding Description of the Coupled Defect Modes in Three-Dimensional Photonic Crystals, Phys. Rev. Lett. **84**, 2140 (2000).
[68] M. J. Collett and C. W. Gardiner, Squeezing of intracavity and traveling-wave light fields produced in parametric amplification, Phys. Rev. A **30**, 1386 (1984).
[69] S. R.-K. Rodriguez, Classical and quantum distinctions between weak and strong coupling, Eur. J. Phys. **37**, 025802 (2016).
[70] L. Novotny, Strong coupling, energy splitting, and level crossings: A classical perspective, Am. J. Phys. **78**, 1199 (2010).
[71] H. Choi, M. Heuck, and D. Englund, Self-Similar Nanocavity Design with Ultrasmall Mode Volume for Single-Photon Nonlinearities, Phys. Rev. Lett. **118**, 223605 (2017).